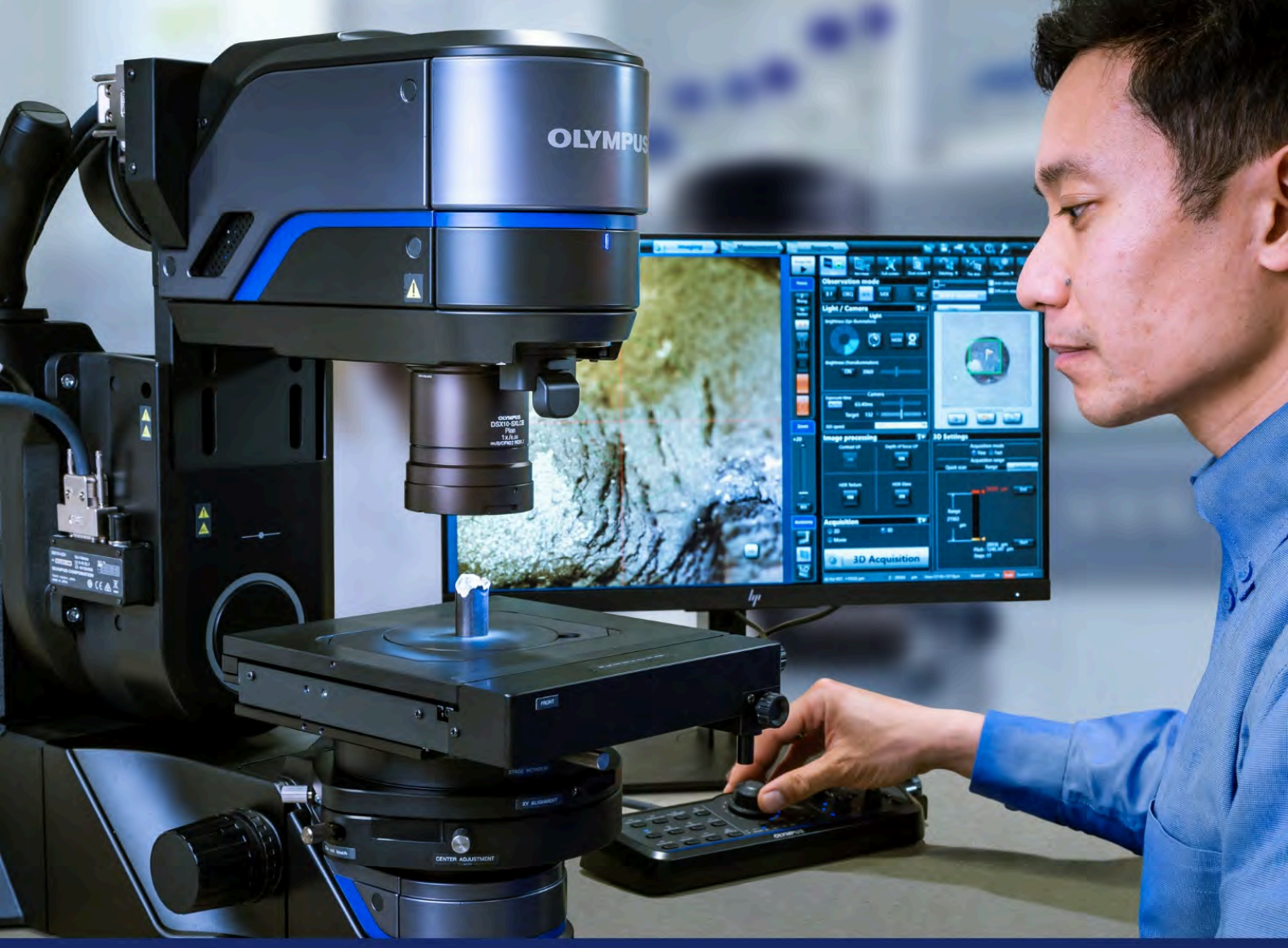

Science Meets Technology with Advanced Optical Metrology

Access in-depth information on methods and applications in the R&D field of optical metrology through free to access article digests of recent peer-reviewed publications and more.

Discover advancedopticalmetrology.com now!

OLYMPUS

WILEY

ADVANCED ENERGY MATERIALS
www.advenergymat.de

Surface-Guided Formation of Amorphous Mixed-Metal Oxyhydroxides on Ultrathin MnO_2 Nanosheet Arrays for Efficient Electrocatalytic Oxygen Evolution

Ming Fang, Dong Han, Wen-Bo Xu, Yun Shen, Youming Lu, Peijiang Cao, Shun Han, Wangying Xu, Deliang Zhu, Wenjun Liu, and Johnny C. Ho**

Earth-abundant amorphous nanomaterials with rich structural defects are promising alternative catalysts to noble metals for an efficient electrochemical oxygen evolution reaction; however, their inferior electrical conductivity and poor morphological control during synthesis hamper the full realization of their potency in electrocatalysis. Herein, a rapid surface-guided synthetic approach is proposed to introduce amorphous and mixed-metal oxyhydroxide overlayers on ultrathin Ni-doped MnO_2 (Ni—MnO_2) nanosheet arrays via a galvanic replacement mechanism. This method results in a monolithic 3D porous catalyst with a small overpotential of only 232 mV to achieve a current density of 10 mA cm^{-2} in 1 M KOH, which is much lower than the corresponding value of 307 mV for the Ni—MnO_2 reference sample. Detailed structural and electrochemical characterization reveal that the unique Ni—MnO_2 ultrathin nanosheet arrays do not only provide a large surface area to guide the formation of active amorphous catalyst layers but also ensure the effective charge transport owing to their high electron conductivity, collectively contributing to the greatly improved catalyst activity. It is envisioned that this highly operable surface-guide synthetic strategy may open up new avenues for the design and fabrication of novel 3D nanoarchitectures integrated with functional amorphous materials for broadened ranges of applications.

1. Introduction

The increasing energy consumption and environmental problems urge the development of clean energy resources. As a clean and carbon-neutral energy carrier, hydrogen has been proposed as an appealing alternative to fossil fuels. In the ideal scenario, hydrogen is produced through water splitting driven by a renewable and clean source of energy, such as solar and wind power.[1–4] Generally, water splitting is proceeded through two fundamental half-reactions: the hydrogen evolution reaction (HER) at the cathode and the water oxidization reaction, also known as the oxygen evolution reaction (OER), at the anode. As compared with HER, the process of OER involves more complicated electron transfer processes, which leads to sluggish kinetics and sets a bottleneck for the energy-efficient full water splitting.[5] Precious metal oxides, such as IrO_2 and RuO_2, are then employed as active electrocatalysts for OER that can accelerate the reaction rate reducing energy consumption; however, their applications are limited to small scales owing to their high-cost, scarcity, and low stability under the working conditions.[6,7] Therefore, tremendous research effort has been devoted to the exploration of alternative electrocatalysts by utilizing low-cost earth-abundant metals.[8–13] To date, a variety of earth-abundant materials, particularly metal oxide/hydroxide based on first-row transition metal elements including Ni, Co, Fe, and Mn, have been demonstrated as promising OER catalysts.[13,14] For example, their amorphous counterparts have the superior activities for OER catalysis because of the lattice distortion and surface dangling bonds that are favorable for the generation of catalytically active *OOH intermediates, which are essential for the OER process.[15–20] In addition, owing to the relative loose packing of atoms, amorphous electrocatalysts possess the high structural flexibility, enabling the catalytically active sites to adjust to any geometry required for electrocatalysis.[21] Moreover, due to the structural disorder, foreign atoms can be easily incorporated into an amorphous phase to form a hybrid catalyst there

Dr. M. Fang, D. Han, W.-B. Xu, Y. Shen, Prof. Y. Lu, Dr. P. Cao, Dr. S. Han, Dr. W. Xu, Prof. D. Zhu, Prof. W. Liu
Shenzhen Key Laboratory of Special Functional Materials
Guangdong Research Center for Interfacial Engineering of Functional Materials
College of Materials Science and Engineering
Shenzhen University
1066 Xueyuan Avenue, Nanshan District, Shenzhen 518060, China
E-mail: Liuwj@szu.edu.cn
Prof. J. C. Ho
Department of Materials Science and Engineering
City University of Hong Kong
Tat Chee Avenue, Kowloon, Hong Kong SAR 999077, China
E-mail: johnnyho@cityu.edu.hk
The ORCID identification number(s) for the author(s) of this article can be found under https://doi.org/10.1002/aenm.202001059.

DOI: 10.1002/aenm.202001059

with synergistically improved catalytic characteristics.[22] Apart from all these advantages, amorphous catalysts often suffer from their low electrical conductivities that restrict the further improvement of their catalytic performances. Also, the loading of amorphous catalysts on electrodes usually requires the use of nonconductive polymer binders, which inevitably leads to poor interparticle connections and eventually causes compromised performances. In this regard, direct growth of nanostructured catalysts on conductive 3D substrates would offer an effective approach to alleviate all these above-mentioned issues.[23] Unfortunately, it is still difficult to achieve the controllable growth of amorphous nanomaterials with predesigned aspect ratio and orientations as a result of the lack of crystalline lattice.

In this work, we demonstrate a facile surface-guided method to fabricate active amorphous catalyst layers by utilizing nickel foam (NF)-supported ultrathin Ni-doped MnO_2 (Ni—MnO_2) nanosheet arrays as the starting material. Then, there is a surface reconstruction process initiated by a simple galvanic replacement reaction between Fe^{2+} and MnO_2 nanosheets in a $FeSO_4$ solution at room temperature, which facilitates the rapid formation of amorphous mixed-metal oxyhydroxide (denoted as ammo@MnO_2) overlayers on the nanosheets by selective dissolution of Mn and simultaneously precipitation of Ni and Fe on the surface. It is impressive that the obtained ammo@MnO_2 catalysts require an overpotential of only 232 mV to achieve a current density of 10 mA cm^{-2} in 1 M KOH, which is much smaller than the corresponding values of 307 and 338 mV for the reference samples of Ni—MnO_2 and NF, respectively. Importantly, the ammo@MnO_2 catalyst also exhibits the high stability for OER under alkaline conditions, delivering a stable overpotential for at least 40 h at a current density of 100 mA cm^{-2} in the chronopotentiometry test.

2. Results and Discussion

The preparation of ammo@MnO_2/NF was achieved via a two-step method, including the in situ hydrothermal growth of ultrathin Ni—MnO_2 nanosheet arrays on NF, followed by a short-time (30s) immersion treatment in an aqueous solution of $FeSO_4$ for the deposition of amorphous (Ni, Fe)-containing, mixed-metal (oxy)hydroxide on the Ni—MnO_2 nanosheet surface as detailed in the Experimental Section. The formation mechanism is illustrated in **Scheme 1**. During the solution treatment, galvanic replacement reactions occurred between Ni—MnO_2 and Fe^{2+} due to the difference in standard redox potentials (E^0) of the FeOOH(s)/Fe^{2+} (0.74 V) and MnO_2(s)/Mn^{2+} (1.23 V) couples, where the solid-state Mn(IV) was reduced to dissolutive Mn^{2+} by Fe^{2+} under the assistance of H^+, producing Fe^{3+} and OH^- simultaneously and then leading to the oxidative deposition of Fe^{3+} in the form of oxide or oxyhydroxide.[24,25] Meanwhile, the released Ni^{2+} or Ni^{3+} species from Ni—MnO_2 would also get reprecipitated with OH^- on the surface.

In this work, ultrathin birnessite-type MnO_2 (δ-MnO_2) nanosheets arrays were grown on a piece of commercial NF by the hydrothermal method in a $KMnO_4$ aqueous solution. Scanning electron microscope (SEM) images confirm the uniform coating of ultrathin nanosheets on the nickel substrate (Figure S1, Supporting Information) similar to those as

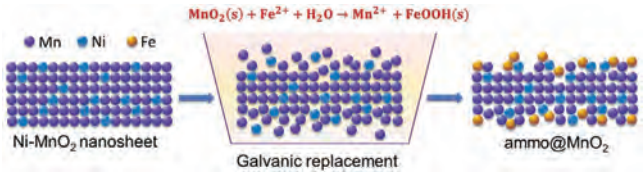

Scheme 1. Process of the surface-guided formation of ammo@MnO_2 via the galvanic replacement reaction.

reported.[26] The layered microstructures were further identified in the transmission electron microscope (TEM) image as shown in **Figure 1**a. The corresponding selected area electron diffraction (SAED) pattern (Figure 1b) shows a typical polycrystalline nature of the nanosheets with three predominant diffraction rings which can be indexed to the (200), (201), and ($\bar{1}$14) atomic planes of the δ-MnO_2 structure (PDF#80-1098), respectively. Through high-resolution TEM (HRTEM), well-defined atomic layers with an interlayer spacing of about 0.695 nm were observed (Figure 1c), corresponding to the (001) atomic planes of δ-MnO_2. Moreover, at the middle region of the shown nanosheet, the (111) planes of δ-MnO_2, with a lattice spacing of 0.227 nm, have also been clearly resolved (Figure 1d). Careful investigation on isolated nanosheets in TEM coupled with energy dispersive X-ray (EDS) spectrum further disclosed that a considerable amount of Ni has been incorporated into the MnO_2 nanosheets, with the atomic ratio of Mn:Ni:K = 33:4:9, while all of the constituent elements are uniformly distributed in the nanosheets (Figure S2, Supporting Information). The Ni is likely originated from the nickel foam during the hydrothermal synthesis. Specifically, the E^0 of the Ni^{2+}/Ni(s) and MnO_4^-/MnO_2(s) couples are −0.236 and 1.692 V, respectively, which allows the nickel substrate to release Ni^{2+} that can be subsequently incorporated into the MnO_2 nanosheets during the hydrothermal process. Notably, Elshof et al.[27] have recently revealed that the atomic-level substitutional doping of 3d metal ions (Co, Fe, Ni) in ultrathin MnO_2 nanosheets can introduce new electronic states near the Fermi level. This way, the electronic conductivity of the material can be enhanced, which implies that the incorporation of Ni would be beneficial for efficient charge transfer in OER catalysis. At the same time, these Ni dopants can provide metal sources for the formation of amorphous mixed oxyhydroxides on the nanosheet surface.

The ammo@MnO_2 catalysts were as well comprehensively characterized. SEM shows that the samples have preserved the layered microstructure without any noticeable degradation (Figure S3, Supporting Information). However, further investigation in TEM clearly reveals that surfaces of the nanosheets become evidently roughened as compared to that of Ni—MnO_2 (Figure 1e). As depicted in the HRTEM images (Figure 1g,h), significant lattice disturbance has also been observed, making it difficult to identify the lattice fringes. The SAED pattern (Figure 1f, corresponding to Figure 1e) presents no structural change except the appearance of the diffraction ring at the innermost position, corresponding to (002) plane of the δ-MnO_2. These observations suggest that while the surfaces of nanosheets have been significantly modified, the main birnessite structure is still largely preserved as the skeleton, whereas no other crystalline phase was formed during the solution treatment. EDS spectrum (Figure S4, Supporting

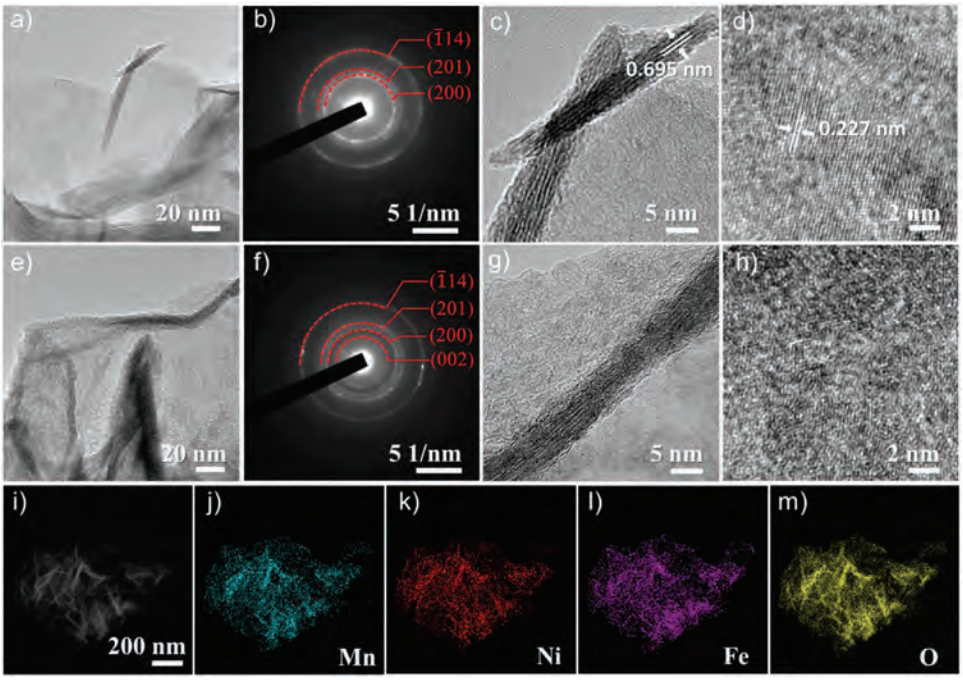

Figure 1. a) SEM image, b) SAED pattern, and c,d) HRTEM images of Ni—MnO_2; e) SEM image, f) SAED pattern, and g,h) HRTEM images of ammo@MnO_2. i) HAADF-STEM image and j–m) the corresponding elemental mapping of Mn, Ni, Fe, and O in ammo@MnO_2.

Information) confirms the precipitation of Fe with an atomic ratio of Mn:Ni:Fe:K being 12.3:5.9:7.6:1.5. The decreased Mn/Ni ratio indicates the loss of Mn in content and the enrichment of Ni on the surface, which is consistent with the mechanism as proposed in Scheme 1. Figure 1i–m displays the high-angle annular dark field-scanning transmission electron microscopy (HAADF-STEM) and the corresponding EDS mapping images. As can be seen, the Mn, Fe, and Ni elements are uniformly distributed in the nanosheets. All these results evidently indicate the formation of Ni—Fe-containing amorphous overlayers on the Ni—MnO_2 nanosheets.

X-ray photoelectron spectroscopy (XPS) was next employed to evaluate the surface chemical bonding states of the samples. The high-resolution Mn 3s spectra were utilized to distinguish the Mn oxidation states. As shown in **Figure 2**a, both Ni—MnO_2 and ammo@MnO_2 exhibit two multiplet-splitting peaks, with a binding energy (B.E.) separation (ΔE_{3S}) of 4.5 eV between the peaks, indicating that Mn existed mainly in the Mn^{4+} state.[28] The high-resolution Mn 2p spectra were also measured and displayed in Figure S5 (Supporting Information). Unfortunately, the overlapping of strong Ni Auger signals (as indicated by the evident observation of $2p_{3/2}$ to $2p_{1/2}$ intensity ratio being larger than 2:1) makes it difficult to apply a quantitative analysis of the peaks, especially for the ammo@MnO_2 sample.[29,30] In any case, the pronounced Ni Auger peak intensity in ammo@MnO_2 implies the increased exposure of Ni substrate due to the removal of MnO_2 during the Fe^{2+} treatment. The Ni 2p spectra (Figure 2b) consist of two peaks for the Ni $2p_{3/2}$ and Ni $2p_{1/2}$ components and their shake-up satellites. Peak fitting reveals the coexistence of Ni^{2+} (856.0, 873.4 eV) and Ni^{3+} (857.0, 875.0 eV) in both of the samples.[31–33] Meanwhile, ammo@MnO_2 has a higher Ni^{3+}/Ni^{2+} peak intensity ratio as compared with the one of the original Ni—MnO_2. It is not surprising to have Ni^{3+} species in the samples, as the oxidation of Ni^{2+} into Ni^{3+} at the surface was feasible given that the E^0 of NiOOH(s)/$Ni(OH)_2$(s) is 0.49 V, being much lower than the one of MnO_4^-/MnO_2(s). In addition, during the Fe^{2+} solution treatment, the redox reaction between the Fe^{2+} and Ni—MnO_2 produced Fe^{3+}-based species, which also held the capacity to oxidize Ni^{2+} into Ni^{3+} and yielded to increased Ni^{3+}/Ni^{2+} atomic ratio in the ammo@Ni—MnO_2 sample. Notably, it has been proposed that Ni^{3+}-rich surfaces can benefit the formation of NiOOH as active sites for OER.[18,34,35] The Fe 2p spectrum (Figure 2c) of ammo@MnO_2 shows two dominant peaks at 712.4 and 725.9 eV corresponding to Fe $2p_{3/2}$ and Fe $2p_{1/2}$, respectively. The B.E. difference of 13.5 eV between the Fe $2p_{3/2}$ and Fe $2p_{1/2}$ peaks as well as the appearance of a peak at 57.1 eV in the Fe 3p spectrum (Figure S6, Supporting Information) consistently indicate the presence of Fe^{3+}.[36] The Fe 2p spectrum was further deconvoluted into two pairs of doublets which could be assigned to Fe^{3+} in the oxide (711.9, 725.2 eV) and oxide–hydroxide (714.0, 727.7 eV) forms, accordingly.[37,38] The O 1s spectra (Figure 2d) exhibited three peaks at 531.0, 532.6, and 535.1 eV, which can be attributed to O^{2-}, OH^-, and adsorbed molecular water, respectively. As contrasted to Ni—MnO_2, the ammo@MnO_2 sample exhibits the greatly improved OH^- peak intensity, indicating the formation of metal (oxy)hydroxide on the surface.

To further shed light on the coordination environment of the atoms in the samples, synchrotron X-ray absorption spectroscopy was performed here. **Figure 3**a displays the normalized Mn K-edge X-ray absorption near edge structure (XANES) profiles of Ni—MnO_2 and ammo@MnO_2. It is clear that both samples present a very similar feature in the absorption profiles except a gentle shift of the absorption edge toward

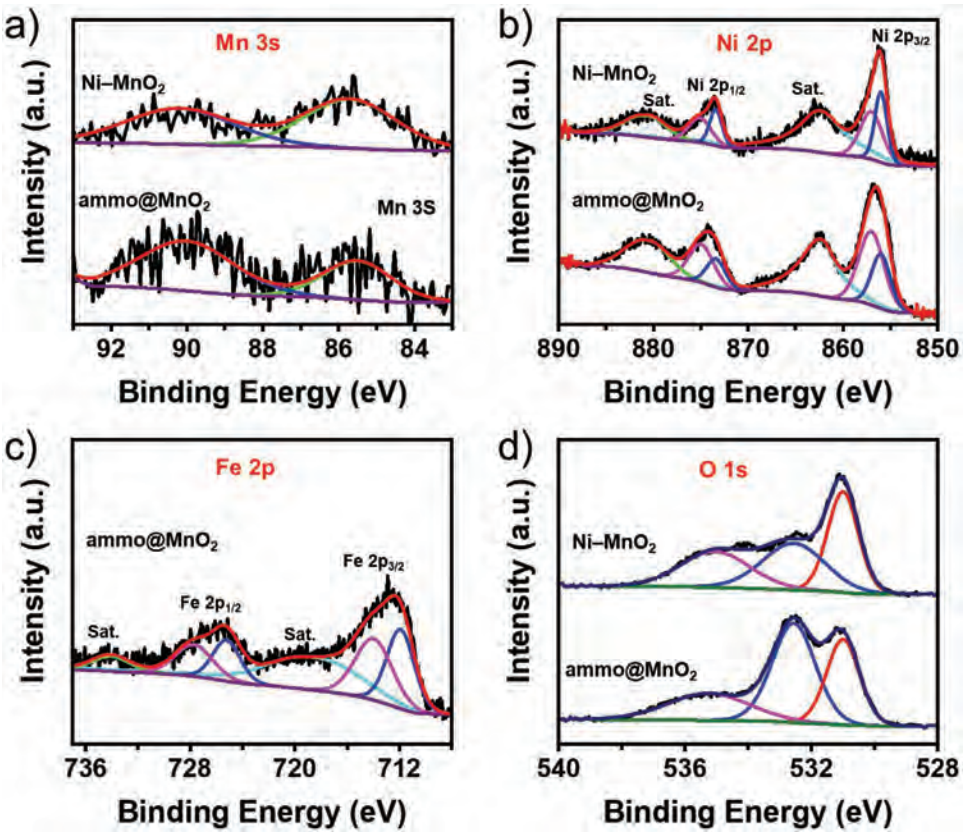

Figure 2. XPS spectra of a) Mn 3s, b) Ni 2p, c) Fe 2p, and d) O1s regions for Ni—MnO_2 and ammo@MnO_2, respectively.

the lower energy for ammo@MnO_2, which indicates the slightly lower average oxidation state of Mn in the sample. By utilizing the linear correlation between the K-edge excitation energy and the metal valence, the average oxidization state of Mn of ammo@MnO_2 and Ni—MnO_2 were determined to be 3.81 and 3.73 (Figure S7, Supporting Information), respectively, which are quite close to the results obtained by XPS. The Fourier transform (FT) extended X-ray absorption fine structure (EXAFS) spectra of samples were obtained from the normalized Mn k-edge curves. As shown in Figure 3b, both samples exhibit two main coordination peaks in the R-space spectra corresponding to the Mn—O and Mn—Mn scattering shells, respectively. The EXAFS data were further fitted in the Artemis software, while the involving parameters are summarized in Table S1, Supporting Information. It is revealed that the average distance of Mn—O and Mn—Mn scattering shells of both samples is kept at 1.90 and 2.87 Å, correspondingly. The coordination numbers (CN) of Mn—O and Mn—Mn are found to be 4.6 and 4.7 for the sample of Ni—MnO_2, whereas the corresponding values are determined as 4.4 and 4.7 for the sample of ammo@MnO_2. This insignificant change of CN implies that the removal of Mn atoms from the lattice most likely proceeded in a layer-by-layer fashion so that the remaining MnO_2 in ammo@MnO_2 being able to maintain in a similar coordination environment. Yet, the larger Debye–Waller factor of ammo@MnO_2 still manifests more structural distortions of the Mn centers in the sample. Notably, the CN of Mn—Mn being less than 6 indicates the presence of coordinatively unsaturated sites in the lattice. The previous study by Xie et al.[39] has demonstrated that this kind of defects in ultrathin MnO_2 nanosheets can lead to a half-metallic property and improve the electron conductivity of the materials, which is beneficial for effective charge transport in OER catalysis. Figure 3c,d displays the normalized Fe K-edge XANES and FT-EXAFS profiles of ammo@MnO_2. The bond length of 1.98 Å and the CN of 6.0 for Fe—O signifies that the Fe atoms are in the octahedral (FeO_6) coordination structure, and meanwhile the CN for Fe—M (M = Fe, Mn, or Ni) is 4.1, being much smaller than the standard value of 6, suggests a considerable amount of FeO_6 octahedrons are coordinatively unsaturated and settled at the edge or out-of-plane positions. The much longer bond length of Fe—M (3.08 Å) with respective to Mn—Mn (2.87 Å) also suggests that the Fe atoms are not incorporated in the Mn—O networks. It is also noteworthy that owing to the strong absorption of Ni metal substrate, there is not any useful information obtained by analyzing the Ni K-edge spectra.

The OER electrocatalytic activity of the monolithic NF-supported ammo@MnO_2 catalysts was investigated by using a standard three-electrode setup in 1 M KOH aqueous solution together with Ni—MnO_2 and bare NF as the reference samples. **Figure 4**a displays the iR-corrected linear sweep voltammetry (LSV) polarization curves of the samples recorded after 20 cyclic voltammetry (CV) treatment. A significant shift of the LSV curve for ammo@MnO_2 toward the less positive potential direction, indicating a remarkable enhanced catalytic activity of the sample. Figure 4b displays a quantitative comparison of the overpotentials required for the three catalysts to achieve the

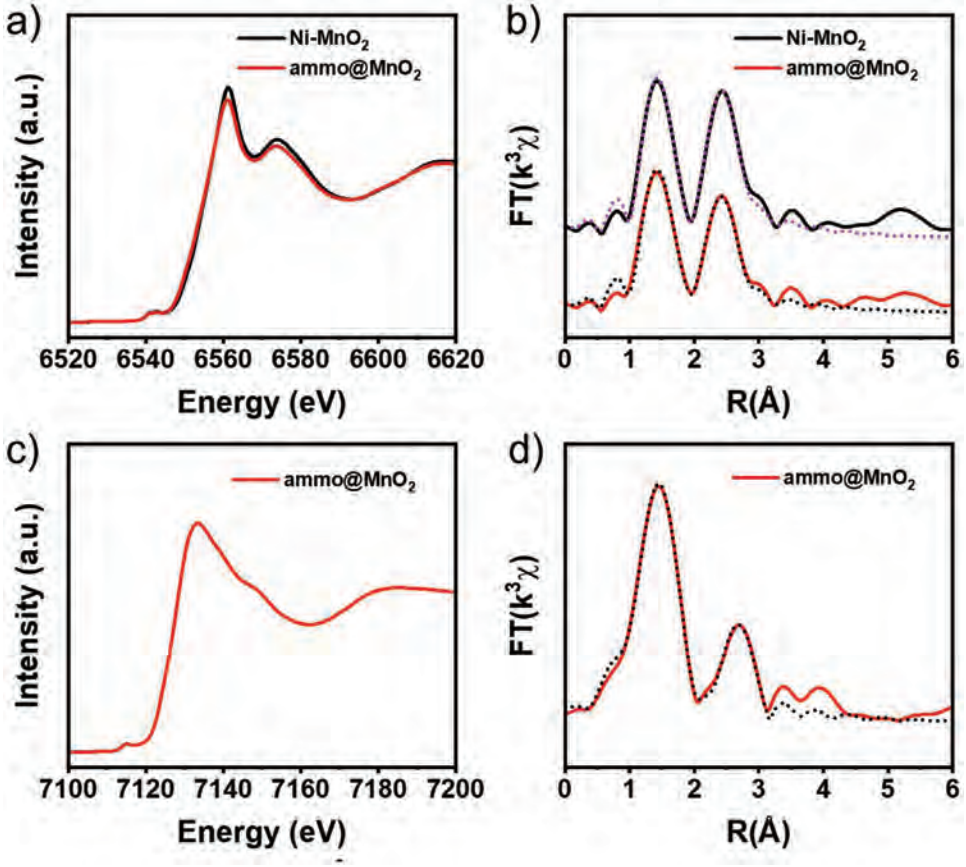

Figure 3. a) XANES spectra and b) k^3-weighted FT-EXAFS of Mn K-edge for Ni—MnO_2 and ammo@MnO_2; c) XANES spectra and d) k^3-weighted FT-EXAFS of Fe K-edge for Ni—MnO_2 and ammo@MnO_2.

current densities of 10, 50, and 100 mA cm^{-2}. As can be seen, in order to obtain a current density of 10 mA cm^{-2}, ammo@MnO_2 requires an overpotential of only 232 mV, which is much lower than the values of 307 and 338 mV for Ni—MnO_2 and NF, respectively. Moreover, ammo@MnO_2 exhibits unique advantages for working at large current densities. For example, at 100 mA cm^{-2}, the required overpotential of ammo@MnO_2 is 270 mV, corresponding to reduced amplitudes of 120 and 193 mV as compared to those of Ni—MnO_2 (390 mV) and NF (463 mV), accordingly. A zoomed view of the LSV curves at the low potential region is presented (Figure S8, Supporting Information) to disclose more detailed information about the electrochemcial characteristics of catalysts. For NF, anodic peaks at 1.34 and 1.36 V are related to change of the Ni oxidation state from Ni^{2+} to Ni^{3+}, where $Ni(OH)_2$ and/or NiO species are oxidized into NiOOH.[40,41] The Ni—MnO_2 exhibits two prominent peaks. The board peak at 0.8-1.2 V is likely due to Mn^{2+}/Mn^{3+} and Mn^{3+}/Mn^{4+} oxidation transitions.[42] The other peak centered at 1.33 V can be ascribed to the oxidizaiton of Ni^{2+} to Ni^{3+}, in which the slight downshift of the peak position as compared to that of NF may suggest the easier oxidative transition of Ni^{2+} in Ni—MnO_2 toward the higher valence. For ammo@MnO_2, the Ni anodic peak is significantly supressed, which has also been observed in iron-contaminated nickel-based OER catalysts, indicating the intimate contact between Ni and Fe atoms.[43,44] Tafel plots are then utilized to analyze the reaction kinetics of associated OER processes. As displayed in Figure 4c, the Tafel slope of ammo@MnO_2 is found to be 36.0 mV dec^{-1}, while the reference samples of Ni—MnO_2/NF and NF give the much larger values of 77.0 and 88.1 mV dec^{-1}, respectively. Typically, the OER process proceeds through four elemental steps associating with active sites, in the sequence of *OH → *O→ *OOH→ O_2, where * represents the active site.[45] According to the previous studies,[46] when the Tafel slope has a value between 30 to 80 mV dec^{-1}, *OH formation is found to be more favorable on the catalyst surface. In the present case, the relatively small Tafel slope of ammo@MnO_2 is possibly resulted from the improved OH^- adsorption capacity by defects and disorder on the catalyst surface, being similar to those proposed in other amorphous material systems.[26,37,47,48] The excellent performance, as indicated by the low overpotential (at 10 mA cm^{-2}) and small Tafel slope, makes ammo@MnO_2 being comparable to the state-of-the-art OER electrocatalysts (Table S3, Supporting Information). Electrocatalytic stability of ammo@MnO_2 was also evaluated by chronopotentiometry (*V–t*) tests at both moderate (10 mA cm^{-2}) and large (100 mA cm^{-2}) current densities. As presented in Figure 4d, there is a slight increase in the overpotential for the initial 10 h test at 10 mA cm^{-2}, which is presumably due to the partial blockage of some active sites by small adhered O_2 gas bubbles; however, in the following 40 h

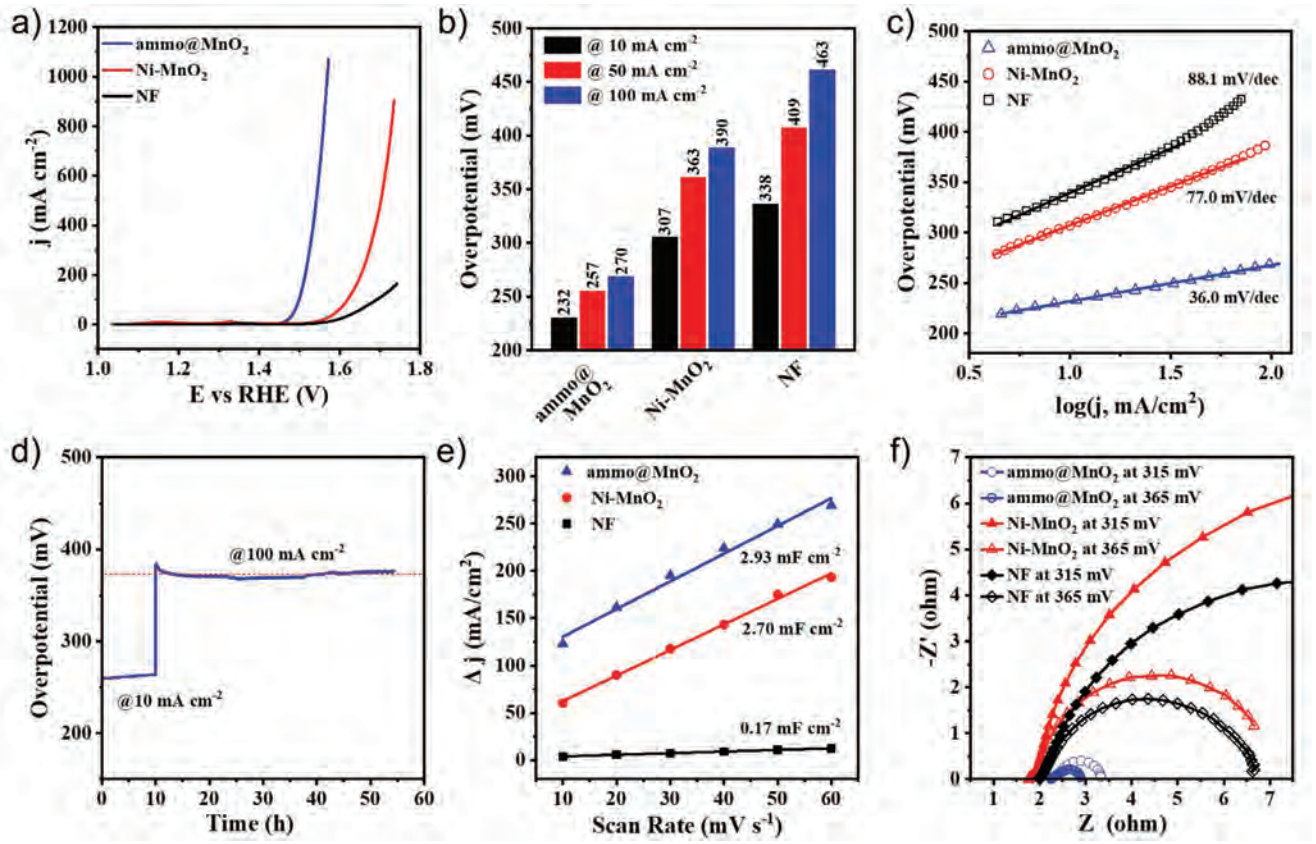

Figure 4. a) iR-corrected LSV polarization curves of NF, Ni—MnO_2, and ammo@MnO_2 electrodes; b) Overpotentials required for j = 10, 50, 100 mA cm^{-2} of the tested electrodes; c) Tafel plots of NF, Ni—MnO_2, and ammo@MnO_2 electrodes; d) Chronopotentiometric measurement on ammo@MnO_2 for OER at the current densities of 10 and 100 mA cm^{-2}; e) Capacitive current density versus scan rate for NF, Ni—MnO_2, and ammo@MnO_2; and f) EIS Nyquist plots of NF, Ni—MnO_2, and ammo@MnO_2 electrodes under the overpotential of 315 and 365 mV for OER. All tests were carried out in 1 M KOH solution.

test at 100 mA cm^{-2}, the overpotential sustains at a voltage of around 373 mV (without iR compensation), demonstrating the excellent durability of the ammo@MnO_2 catalyst.

Since the activity of a catalyst is controlled by both the number of active sites and the intrinsic activity of each site, it is important to investigate the electrochemically active surface area (ECSA) to estimate the number of exposed active sites and evaluate the intrinsic activity. The double-layer capacitance (C_{dl}), which is proportional to the ECSA, was obtained by CV measurements under different scanning rates in a nonfaradaic potential window. Figure 4e shows the capacitive current densities as a function of scanning rate extracted from the CV curves presented in Figure S9, Supporting Information. The linear slope of each the data set is equivalent to twice of the double-layer capacitance C_{dl}. The calculated C_{dl} values of ammo@MnO_2, Ni—MnO_2, and NF are found to be 2.93, 2.70, and 0.17 mF cm^{-2}, respectively. By taking the average C_{dl} value of 40 μF cm^{-2} for a smooth metal surface, the roughness factor (σ) of ammo@MnO_2, Ni—MnO_2, and NF can be calculated as 73.3, 67.5, and 4.25, correspondingly. The intrinsic activities of the catalysts can be reliably compared by normalizing the polarization curves with respect to the roughness factors. As displayed in Figure S10 in the Supporting Information, at any given normalized current density, the ammo@MnO_2 catalysts always exhibit the smallest overpotential, confirming their high intrinsic catalytic activity. Notably, the LSV curve of Ni—MnO_2 lags behind the one of NF after the normalization, implying that the increased surface area of Ni—MnO_2 plays the essential role in its catalytic activity improvement. Electrochemical impedance spectroscopy (EIS) was also employed to further assess the catalytic kinetics of the samples. Figure 4f shows the Nyquist plots of ammo@MnO_2 and the reference samples measured at the overpotential of 315 and 365 mV. Apparently, all the samples exhibit a potential-dependent radius of the semicircles, which reflects the change of charge transfer resistance (R_{ct}) at different potential levels. The data were further fitted by applying an equivalent circuit (Figure S11, in the Supporting Information) consisting of a solution resistance (R_s) connected in series with two parallel combinations of resistors (R_1, R_{ct}) and constant-phase elements (CPE_1, CPE_2), where the R_1-CPE_1 time constant simulates the charge transfer at the NF/catalyst junction and the R_{ct}-CPE_2 represents the charge transfer process at the catalyst/electrolyte interface. The obtained values of R_s, R_1, and R_{ct} are summarized in Table S2, Supporting Information. It is not surprising that bare NF has the smallest R_1 of 0.05 Ω owing to its metallic nature. The R_1 of ammo@MnO_2 (0.29 Ω) is larger than that of Ni—MnO_2 (0.15 Ω), signifying the relatively lower conductivity of the amorphous oxyhydroxide layer. Nevertheless, these values are still within the reasonable range, which indicates the effectiveness of our structural design strategy by

utilizing the more conductive Ni—MnO_2 nanosheet arrays as the supporting skeleton. The R_{ct} of ammo@MnO_2 is 0.81 Ω at the overpotential of 315 mV, while the corresponding values for Ni—MnO_2 and NF are determined to be 15.28 and 11.95 Ω. The much smaller R_{ct} value indicates the faster charge transfer rate between its surface and reaction intermediates, confirming the higher intrinsic catalytic activity of ammo@MnO_2 among all the measured samples. Meanwhile, the R_{ct} of Ni—MnO_2 is slightly larger than that of NF, which coincides well with the results of normalized LSV curves (Figure S10, Supporting Information) as mentioned above, suggesting the important role of Ni atoms for OER catalysis.

Based on the above analyses, the high performance of NF-supported ammo@MnO_2 catalysts can be understood from the following aspects. First, the formation of homogeneously mixed-metal oxyhydroxide plays an essential role in increasing the intrinsic catalytic activity. It is speculated that the synergistic interplay between Mn, Fe, and Ni produces the favorable local coordination environment and electronic structure that optimizes the adsorption energies of oxygen evolution intermediates and hence reduces the required overpotential.[49,50] Such an effect has been previously demonstrated in both Fe—Mn and Ni—Fe hydroxide material systems.[8,18,37,51–53] Second, the conductive Ni—MnO_2 ultrathin nanosheet arrays do not only provide a large surface area to guide the formation of amorphous catalyst layers but also ensure the effective charge transport due to their superior electron conductivity. Lastly, the hierarchical ammo@MnO_2/NF 3D architecture enables the effective mass transfer, which allows the catalyst to function at high current densities without significant performance compromise.[23]

3. Conclusions

In summary, a facile surface-guided synthetic route has been developed to direct the growth of amorphous mixed-metal oxide (overcoat) layers on ultrathin Ni—MnO_2 nanosheet arrays supported on NF. During the fabrication, the high redox potential of MnO_2/Mn^{2+} provides the driving force for the oxidative deposition of Ni and Fe on the surface in the (oxy)hydroxide form. Electrochemical measurements reveal that the unique ammo@MnO_2/NF electrode delivers a greatly improved catalytic performance for OER in alkaline conditions, requiring an overpotential of only 232 mV to achieve a current density of 10 mA cm^{-2} that is much smaller as compared to the value of 307 mV of Ni—MnO_2 nanosheet arrays. Moreover, ammo@MnO_2/NF also possesses high stability for OER, allowing operation for at least 40 hours at a current density of 100 mA cm^{-2} without degradation. Detailed structural and electrochemical analyses suggest that the superior OER activity of the catalyst can be mainly ascribed to the atomic-scale synergy among the homogeneously mixed Mn, Fe, and Ni atoms. Moreover, the superior conductivity and high electrochemical surface area of the Ni—MnO_2/NF scaffold also ensure the effective charge and mass transfer for electrocatalysis. This surface-guided synthetic approach does not only enable the facile fabrication of a novel OER electrocatalysts with excellent activity but also opens up new avenues for the development of other material systems integrated with functional amorphous materials for various applications.

4. Experimental Section

Preparation of Ni—MnO_2 Nanosheet Arrays Supported on Nickel Foams: Ni—MnO_2/NF was synthesized via an in situ hydrothermal method. Frist, NF was cut into pieces of 2×4 cm^2, washed in isopropyl alcohol and HCl (1 M) sequentially for 10 min, rinsed in deionized water (DI) and ethanol, and then dried under N_2 gas blowing. The washed NF was transferred into a 50 mL of Teflon-lined autoclave containing 50×10^{-3} M aqueous solution of $KMnO_4$. The enclosed autoclave was then heated at 180 °C for 2.5 h in an electric oven. After cooling to room temperature, the Ni—MnO_2/NF product was obtained. The product was washed with distilled water and ethanol several times and then dried in air at 60 °C.

Surface-Guided Formation of ammo@MnO_2 Nanosheets: ammo@MnO_2 nanosheets were fabricated through a galvanic replacement reaction at room temperature. Typically, the Ni—MnO_2/NF was immersed in a freshly prepared 20×10^{-3} M aqueous solution of Fe_2SO_4 for 30 s, rinsed with DI water and ethanol, and then dried under N_2 gas blowing.

Material Characterization: The morphology and chemical composition were investigated by a Hitachi SU8010 field emission SEM and JEOL2100F scanning transmission electron microscopy (STEM). Both of which are equipped with EDS. XPS data were obtained on a Thermo Fisher Scientific ESCALAB X-ray photoelectron spectrometer. The X-ray absorption spectra were collected on the beamline BL01C1 in National Synchrotron Radiation Research Center under the technical support by Ceshigo Research Service. The radiation was monochromatized by a Si (111) double-crystal monochromator. The data were processed and fitted by using the Athena and Artemis software packages.

Electrochemical Measurement: The electrochemical measurements were performed on a Gamry 1010E potential station with a three-electrode cell. The bulky nickel foam supported catalyst was directly used as the working electrode. A piece of pure nickel foam and a saturated calomel electrode (SCE) were employed as the counter and the reference electrode, respectively. The SCE reference electrode was connected with an additional KCl salt bridge before contacting with the KOH electrolyte (as shown in Figure S12, Supporting Information). All electrochemical measurements were conducted in 1 M KOH (pH = 13.6). Potentials were converted to the reversible hydrogen electrode (RHE) scale via the Nernst equation ($E_{\text{vs RHE}} = E_{\text{vs SCE}} + 0.059 * \text{pH} + 0.242$ V $= E_{\text{vs SCE}} + 1.044$ V). The SCE has also been calibrated against a Pt|H_2(g) electrode in the 1 M KOH electrolyte. The potential measured for SCE is 1.045 V (Figure S13, Supporting Information), which is consistent with the one calculated by using the Nernst equation. The work electrodes were subjected to 20 CV scans with a scan rate of 100 mV s^{-1} at the potential range of –0.1–0.7 V versus SCE before data collection. The LSV curves were recorded at a scan rate of 5 mV s^{-1} with iR compensation by applying the current interrupt method. The EIS measurements were performed under potential static mode over the frequency range of 10^{-2}–10^5 Hz at the overpotential (vs 1.23 V) of 315 or 365 mV with the oscillation amplitude of 10 mV.

Supporting Information

Supporting Information is available from the Wiley Online Library or from the author.

Acknowledgements

This work was financially supported by the National Natural Science Foundation of China (Grant Nos. 21805194, 61704111, 51872187, 51371120, and 11774241), the Science and Technology Planning Project of Shenzhen Municipality (Grants Nos. JCYJ20190808141015383 and JCYJ20170818144212483), and the Shenzhen University Initiative Research Program (Grant No. 2019002).

Conflict of Interest

The authors declare no conflict of interest.

Keywords

amorphous, mixed-metal oxyhydroxide, MnO_2, oxygen evolution reaction, ultrathin nanosheets

Received: March 24, 2020
Revised: May 21, 2020
Published online: June 5, 2020

[1] J. A. Turner, *Science* **1999**, *285*, 687.
[2] M. G. Walter, E. L. Warren, J. R. McKone, S. W. Boettcher, Q. Mi, E. A. Santori, N. S. Lewis, *Chem. Rev.* **2010**, *110*, 6446.
[3] J. Jia, L. C. Seitz, J. D. Benck, Y. Huo, Y. Chen, J. W. D. Ng, T. Bilir, J. S. Harris, T. F. Jaramillo, *Nat. Commun.* **2016**, *7*, 13237.
[4] Y. Tachibana, L. Vayssieres, J. R. Durrant, *Nat. Photonics* **2012**, *6*, 511.
[5] I. Katsounaros, S. Cherevko, A. R. Zeradjanin, K. J. J. Mayrhofer, *Angew. Chem., Int. Ed.* **2014**, *53*, 102.
[6] T. Reier, M. Oezaslan, P. Strasser, *ACS Catal.* **2012**, *2*, 1765.
[7] I. Roger, M. A. Shipman, M. D. Symes, *Nat. Rev. Chem.* **2017**, *1*, 0003.
[8] H. Xiao, H. Shin, W. A. Goddard, *Proc. Natl. Acad. Sci. USA* **2018**, *115*, 5872.
[9] G. Dong, M. Fang, J. Zhang, R. Wei, L. Shu, X. Liang, S. Yip, F. Wang, L. Guan, Z. Zheng, J. C. Ho, *J. Mater. Chem. A* **2017**, *5*, 11009.
[10] Z.-F. Huang, J. Song, Y. Du, S. Xi, S. Dou, J. M. V. Nsanzimana, C. Wang, Z. J. Xu, X. Wang, *Nat. Energy* **2019**, *4*, 329.
[11] C. Walter, P. W. Menezes, S. Orthmann, J. Schuch, P. Connor, B. Kaiser, M. Lerch, M. Driess, *Angew. Chem., Int. Ed.* **2018**, *57*, 698.
[12] P. W. Menezes, C. Walter, J. N. Hausmann, R. Beltrán-Suito, C. Schlesiger, S. Praetz, V. Yu. Verchenko, A. V. Shevelkov, M. Driess, *Angew. Chem., Int. Ed.* **2019**, *58*, 16569.
[13] F. Song, L. Bai, A. Moysiadou, S. Lee, C. Hu, L. Liardet, X. Hu, *J. Am. Chem. Soc.* **2018**, *140*, 7748.
[14] C. C. L. McCrory, S. Jung, I. M. Ferrer, S. M. Chatman, J. C. Peters, T. F. Jaramillo, *J. Am. Chem. Soc.* **2015**, *137*, 4347.
[15] R. D. L. Smith, M. S. Prévot, R. D. Fagan, S. Trudel, C. P. Berlinguette, *J. Am. Chem. Soc.* **2013**, *135*, 11580.
[16] A. Indra, P. W. Menezes, N. R. Sahraie, A. Bergmann, C. Das, M. Tallarida, D. Schmeißer, P. Strasser, M. Driess, *J. Am. Chem. Soc.* **2014**, *136*, 17530.
[17] L. Yang, H. Ren, Q. Liang, K. N. Dinh, R. Dangol, Q. Yan, *Small* **2020**, *16*, 1906766.
[18] G. Chen, Y. Zhu, H. M. Chen, Z. Hu, S. Hung, N. Ma, J. Dai, H. Lin, C. Chen, W. Zhou, Z. Shao, *Adv. Mater.* **2019**, *31*, 1900883.
[19] H. Zhang, B. Chen, H. Jiang, X. Duan, Y. Zhu, C. Li, *Nanoscale* **2018**, *10*, 12991.
[20] S. Anantharaj, S. Noda, *Small* **2020**, *16*, 1905779.
[21] J. Liu, J. Nai, T. You, P. An, J. Zhang, G. Ma, X. Niu, C. Liang, S. Yang, L. Guo, *Small* **2018**, *14*, e1703514.
[22] Y. Duan, Z. Yu, S. Hu, X. Zheng, C. Zhang, H. Ding, B. Hu, Q. Fu, Z. Yu, X. Zheng, J. Zhu, M. Gao, S. Yu, *Angew. Chem.* **2019**, *131*, 15919.
[23] M. Fang, G. Dong, R. Wei, J. C. Ho, *Adv. Energy Mater.* **2017**, *7*, 1700559.
[24] D. C. Harris, *Quantitative Chemical Analysis*, W.H. Freeman & Company, New York **2007**.
[25] M. H. Oh, T. Yu, S. H. Yu, B. Lim, K. T. Ko, M. G. Willinger, D. H. Seo, B. H. Kim, M. G. Cho, J. H. Park, K. Kang, Y. E. Sung, N. Pinna, T. Hyeon, *Science* **2013**, *340*, 964.
[26] Y. Zhao, C. Chang, F. Teng, Y. Zhao, G. Chen, R. Shi, G. I. N. Waterhouse, W. Huang, T. Zhang, *Adv. Energy Mater.* **2017**, *7*, 1700005.
[27] Y. Wang, Y.-Z. Zhang, Y.-Q. Gao, G. Sheng, J. E. ten Elshof, *Nano Energy* **2020**, *68*, 104306.
[28] E. Beyreuther, S. Grafström, L. M. Eng, C. Thiele, K. Dörr, *Phys. Rev. B* **2006**, *73*, 155425.
[29] V. Rednic, L. Rednic, M. Coldea, V. Pop, M. Neumann, R. Pacurariu, A. R. Tunyagi, *Cent. Eur. J. Phys.* **2008**, *6*, 434.
[30] A. Papaderakis, N. Pliatsikas, C. Prochaska, K. M. Papazisi, S. P. Balomenou, D. Tsiplakides, P. Patsalas, S. Sotiropoulos, *Front. Chem.* **2014**, *2*, 1.
[31] D. Xiong, W. Li, L. Liu, *Chem. - Asian J.* **2017**, *12*, 543.
[32] Y. Ouyang, R. Huang, X. Xia, H. Ye, X. Jiao, L. Wang, W. Lei, Q. Hao, *Chem. Eng. J.* **2019**, *355*, 416.
[33] T. Zhou, Z. Cao, P. Zhang, H. Ma, Z. Gao, H. Wang, Y. Lu, J. He, Y. Zhao, *Sci. Rep.* **2017**, *7*, 46154.
[34] H. Y. Wang, Y. Y. Hsu, R. Chen, T. S. Chan, H. M. Chen, B. Liu, *Adv. Energy Mater.* **2015**, *5*, 1500091.
[35] Y. Zhao, X. Jia, G. Chen, L. Shang, G. I. N. Waterhouse, L. Z. Wu, C. H. Tung, D. Ohare, T. Zhang, *J. Am. Chem. Soc.* **2016**, *138*, 6517.
[36] T. Yamashita, P. Hayes, *Appl. Surf. Sci.* **2008**, *254*, 2441.
[37] Y. Teng, X.-D. Wang, J.-F. Liao, W.-G. Li, H.-Y. Chen, Y.-J. Dong, D.-B. Kuang, *Adv. Funct. Mater.* **2018**, *28*, 1802463.
[38] Q. Zhou, Y. Chen, G. Zhao, Y. Lin, Z. Yu, X. Xu, X. Wang, H. K. Liu, W. Sun, S. X. Dou, *ACS Catal.* **2018**, *8*, 5382.
[39] H. Wang, J. Zhang, X. Hang, X. Zhang, J. Xie, B. Pan, Y. Xie, *Angew. Chem., Int. Ed.* **2015**, *54*, 1195.
[40] V. Srinivasan, *J. Electrochem. Soc.* **1997**, *144*, L210.
[41] M. S. Wu, H. H. Hsieh, *Electrochim. Acta* **2008**, *53*, 3427.
[42] M. V. Abrashev, P. Chernev, P. Kubella, M. R. Mohammadi, C. Pasquini, H. Dau, I. Zaharieva, *J. Mater. Chem. A* **2019**, *7*, 17022.
[43] M. W. Louie, A. T. Bell, *J. Am. Chem. Soc.* **2013**, *135*, 12329.
[44] L. Trotochaud, S. L. Young, J. K. Ranney, S. W. Boettcher, *J. Am. Chem. Soc.* **2014**, *136*, 6744.
[45] G. Fu, X. Wen, S. Xi, Z. Chen, W. Li, J. Y. Zhang, A. Tadich, R. Wu, D. C. Qi, Y. Du, J. Cheng, K. H. L. Zhang, *Chem. Mater.* **2019**, *31*, 419.
[46] D. A. García-Osorio, R. Jaimes, J. Vazquez-Arenas, R. H. Lara, J. Alvarez-Ramirez, *J. Electrochem. Soc.* **2017**, *164*, E3321.
[47] Y. Li, F.-M. Li, X.-Y. Meng, S.-N. Li, J.-H. Zeng, Y. Chen, *ACS Catal.* **2018**, *8*, 1913.
[48] C. Hu, L. Zhang, Z.-J. Zhao, A. Li, X. Chang, J. Gong, *Adv. Mater.* **2018**, *30*, 1705538.
[49] B. Zhang, X. Zheng, O. Voznyy, R. Comin, M. Bajdich, M. García-Melchor, L. Han, J. Xu, M. Liu, L. Zheng, F. P. G. De Arquer, C. T. Dinh, F. Fan, M. Yuan, E. Yassitepe, N. Chen, T. Regier, P. Liu, Y. Li, P. De Luna, A. Janmohamed, H. L. Xin, H. Yang, A. Vojvodic, E. H. Sargent, *Science* **2016**, *352*, 333.
[50] J. Jiang, F. Sun, S. Zhou, W. Hu, H. Zhang, J. Dong, Z. Jiang, J. Zhao, J. Li, W. Yan, M. Wang, *Nat. Commun.* **2018**, *9*, 2885.
[51] J. Wang, L. Gan, W. Zhang, Y. Peng, H. Yu, Q. Yan, X. Xia, X. Wang, *Sci. Adv.* **2018**, *4*, eaap7970.
[52] J. Bak, H. Bin Bae, S.-Y. Chung, *Nat. Commun.* **2019**, *10*, 2713.
[53] R. D. L. Smith, C. Pasquini, S. Loos, P. Chernev, K. Klingan, P. Kubella, M. R. Mohammadi, D. González-Flores, H. Dau, *Energy Environ. Sci.* **2018**, *11*, 2476.